University of Huddersfield Repository

Kepaptsoglou, Demie, Baran, Jakub D., Azough, Feridoon, Ekren, Dursun, Srivastava, Deepanshu, Molinari, Marco, Parker, Stephen C., Ramasse, Quentin M. and Freer, Robert

Prospects for Engineering Thermoelectric Properties in La1/3NbO3 Ceramics Revealed via Atomic-Level Characterization and Modeling

Original Citation

This version is available at http://eprints.hud.ac.uk/id/eprint/34362/

http://eprints.hud.ac.uk/

Supplementary Information.

Prospects for engineering thermoelectric properties in La$_{1/3}$NbO$_3$ ceramics revealed *via* atomic-level characterization and modelling

Demie Kepaptsoglou[1]*, Jakub D. Baran[2], Feridoon Azough[3], Dursun Ekren[3], Deepanshu Srivastava[3], Marco Molinari[2,4], Stephen C. Parker[2] *, Quentin M. Ramasse[1] and Robert Freer[3]

*Corresponding authors: dmkepap@superstem.org, s.c.parker@bath.ac.uk

[1] SuperSTEM Laboratory, SciTech Daresbury Campus, Daresbury WA4 4AD, U.K.
[2] Department of Chemistry, University of Bath, Claverton Down, Bath BA2 7AY, UK
[3] School of Materials, University of Manchester, Manchester, M13 9PL, U.K.
[4] Department of Chemistry, University of Huddersfield, Huddersfield, HD1 3DH, U.K.

1. X-ray Diffraction refinement

A schematic representation as a ball-and-stick model of the structure obtained from the refinement of the X-ray data is shown in Figure S1.
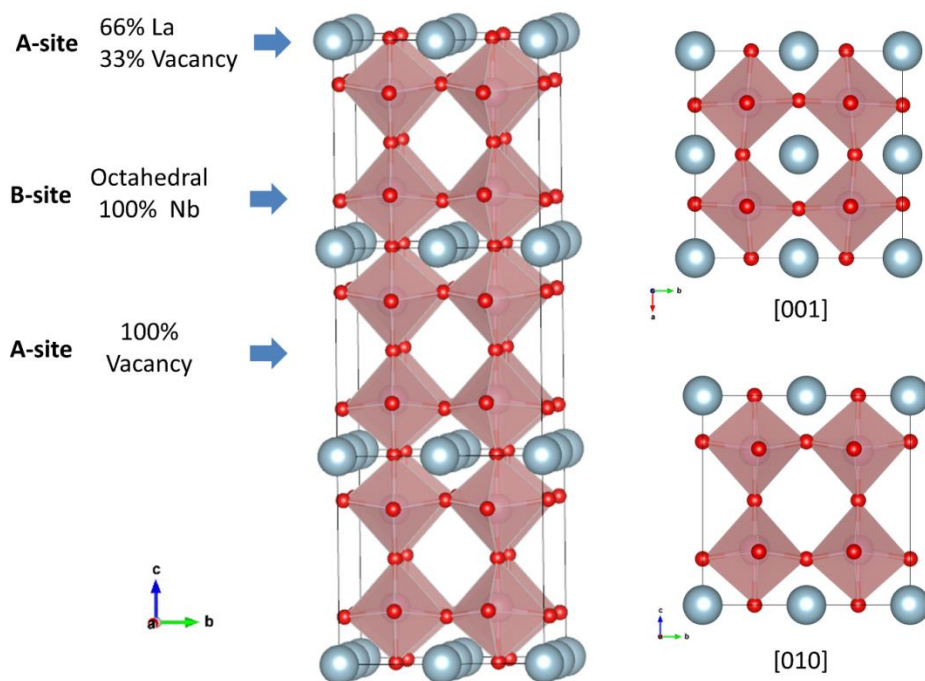

Figure S1: *Schematic representation of the crystal structure of LNO.*

Table S1: *Refined structural data for La$_{1/3}$NbO$_3$.*

From CIF file with ICSD number of 90692[1]			From CIF file with ICSD number of 150448[2]		
Space Group		*Cmmm*	**Space Group**		*Cmmm*
R$_{wp}$/GOF		4.70/3.01	**R$_{wp}$/GOF**		4.71/3.02
Lattice Parameters			**Lattice Parameters**		
a (Å)		7.8159930	**a (Å)**		7.8373086
b (Å)		7.8364456	**b (Å)**		7.8164005
c (Å)		7.9108678	**c (Å)**		7.9110676
V (Å)^3		484.53752	**V (Å)^3**		484.62838
La1			**La1**		
	X	0.0000		X	0.25530
	Y	0.0000		Y	0.0000
	Z	0.0000		Z	0.0000
	b$_{eq}$	1.218		b$_{eq}$	0.765
	Occupancy	0.6803		**Occupancy**	0.6753
La2			**Nb**		
	X	0.0000		X	0.0000
	Y	0.5000		Y	0.26144
	Z	0.0000		Z	0.26083
	b$_{eq}$	1.218		b$_{eq}$	1.104
	Occupancy	0.6012		**Occupancy**	1
Nb			**O1**		
	X	0.2500		X	0.0000
	Y	0.2500		Y	0.30280
	Z	0.26310		Z	0.0000
	b$_{eq}$	1.034		b$_{eq}$	0.5614
	Occupancy	1		**Occupancy**	1
O1			**O2**		
	X	0.0000		X	0.0000
	Y	0.31161		Y	0.19210
	Z	0.26288		Z	0.5000
	b$_{eq}$	1.15		b$_{eq}$	0.5614
	Occupancy	1		**Occupancy**	1
O2			**O3**		
	X	0.23858		X	0.0000
	Y	0.0000		Y	0.0000
	Z	0.22476		Z	0.20190
	b$_{eq}$	1.15		b$_{eq}$	0.5614

	Occupancy	1			**Occupancy**	1
O3				**O4**		
	X	0.2500			X	0.0000
	Y	0.2500			Y	0.5000
	Z	0.0000			Z	0.23590
	b_{eq}	1.15			b_{eq}	0.5614
	Occupancy	1			**Occupancy**	1
O4				**O5**		
	X	0.2500			X	0.2500
	Y	0.2500			Y	0.2500
	Z	0.5000			Z	0.23470
	b_{eq}	1.15			b_{eq}	0.5614
	Occupancy	1			**Occupancy**	1

2. Electron Microscopy:

2.1. Scanning Electron Microscopy (SEM):

A typical back-scattered SEM image for the LNO ceramic is shown in Figure S2. The grains are equiaxed with a narrow grain size distribution; most individual grains are in the 5-10 µm range. The porosity is located at the grain boundaries. Trapped pores within the grains also exist in the microstructure. A secondary phase, indexed as a $LaNbO_4$ oxide can also be found in the microstructure.
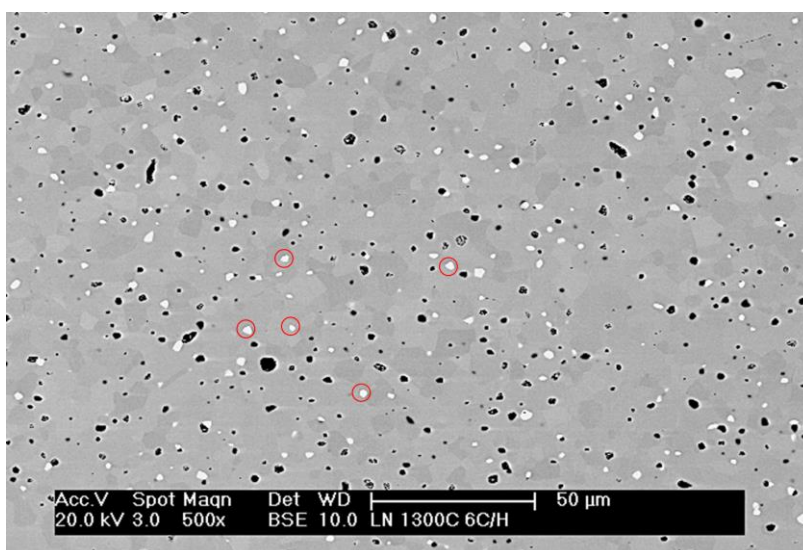

Figure S2. *SEM image of LNO showing grains of $La_{1/3}NbO_3$, the $LaNbO_4$ secondary phase (white grains examples of which are marked by red circles) and the porosity (dark contrast) of the synthesised pellets.*

2.2. High Angle Annular Scanning Transmission Electron Microscopy Imaging (HAADF-STEM) and simulations

HAADF STEM images, such as those presented in Figure 3 of the main text and Figures S3 and S4a herein, are averages of stacks of 50 consecutive, rapidly-acquired HAADF STEM frames, corrected for specimen drift and scanning distortions using non-rigid registration techniques[3] as implemented in the commercially-available SmartAlign Plugin.[4] The images were further corrected for orthogonality using the Jitterbug plugin[5,6].

HAADF image intensity profiles were subsequently produced by integrating the image intensity over several ($\approx$20) unit cells along the b-axis. The relative atomic positions and corresponding relative distances along the c-axis were obtained by fitting the intensity profiles using Gaussian curves and averaging over several measurements. The errors provided correspond to standard deviation values. The average unit cell size along the c-axis was determined to be c $\approx$ 8.07$\pm$0.03 Å in good agreement with the value determined by the refinement of the X-ray diffraction measurements. The relative distance c_1 between B-sites on either side of the partially occupied A_1 cation layer was determined to be $c_1 \approx 3.85 \pm 0.02$ Å, and the distance c_2 between B-sites on either side of the fully-vacant A_2 layer was determined to be $c_1 \approx 4.23 \pm 0.02$ Å (Figure S3).
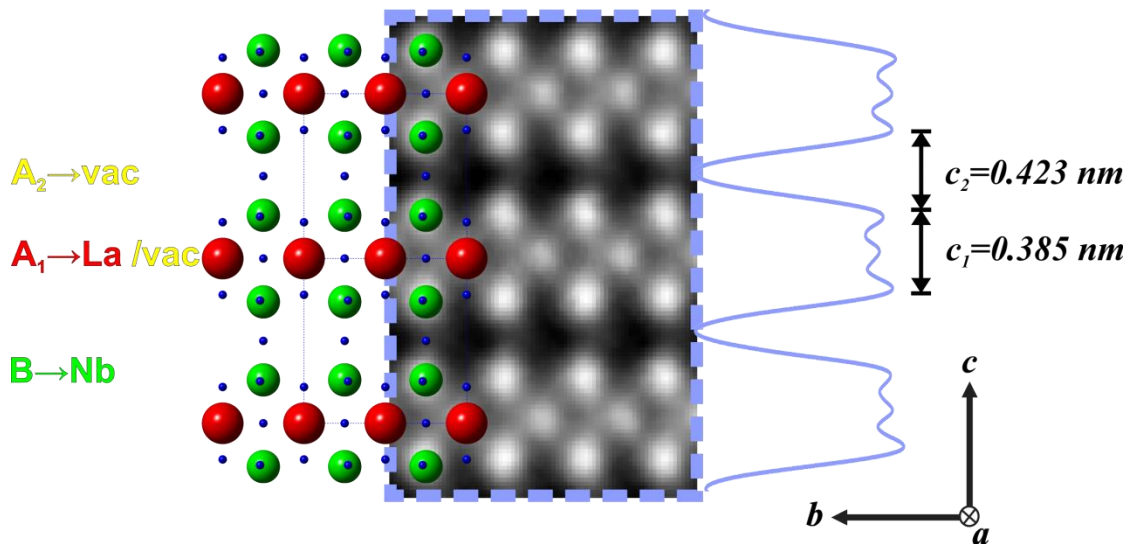

Figure S3: Experimental HAADF STEM image of the LNO ceramic acquired along the [100] zone axis and integrated image intensity profile. The image is a cut-out of the [100] HAADF STEM image shown in Figure 3a – which in turn is an average of 50 consecutive, rapidly-acquired HAADF STEM frames, corrected for specimen drift, scanning distortions and orthogonality.

Supplementary Information:

In order to confirm the structure of the LNO ceramic from HAADF STEM images, multi-slice image simulations were performed using the Dr.Probe[7] simulation package. The parameters used for image simulations (e.g. acceleration voltage, aberration coefficients, acceptance angles, specimen thickness, etc…) reflect the exact experimental conditions under which the LNO ceramic was observed, described in the Methods section of the main text. The structural parameters for the simulations were taken from Ref. [1]

Examination of the HAADF STEM images of the LNO ceramic (Figures S5, S6 and Figure 3 in the main text) reveals that the B-site columns, which are occupied by Nb, show a higher intensity than that of the A-site columns occupied by La. This observation could seem counter-intuitive, especially considering the $\sim Z^2$ dependence of the HAADF STEM image intensity[1]; the columns containing the significantly-heavier La ions are hence expected to appear brighter than the Nb columns($Z_{Nb}^2 = 168 \ vs \ Z_{La}^2 = 3249$). This apparent discrepancy is due to the high vacancy content of the A-site, and is confirmed by multi-slice image simulations (Figure S4).
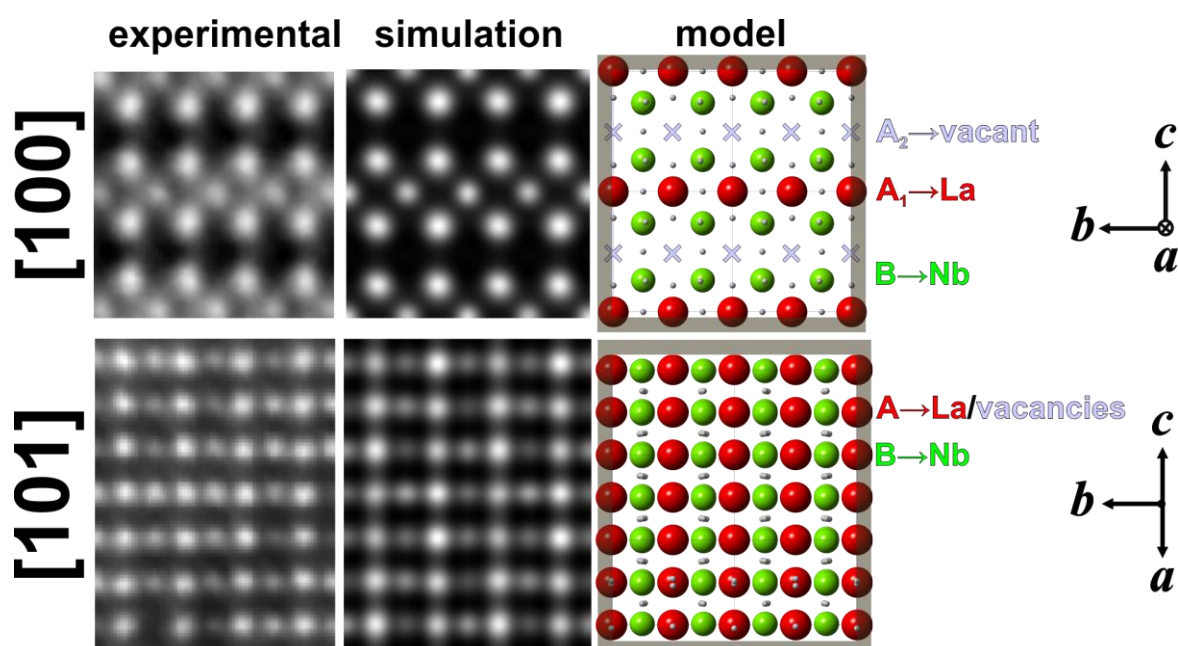

***Figure S4:** Experimental and simulated HAADF STEM images of the LNO ceramic, along the [100] and [101] zone axes, and corresponding ball-and-stick models of the Cmmm structure. The image simulations[7] show that the brighter cation columns in both orientations correspond to the B-site Nd columns, while the darker columns correspond to the partially-*

---

[1] Applies for very thin regions of the sample, for which the image contrast scales, to a good approximation, as the square of the atomic number Z (the actual dependence is closer Z^n, n = 1.6−1.8, here is denoted as $\sim Z^2$ for simplicity)

occupied A-site La columns. In the [100] orientation no A_2-site is observed in the images as it is fully unoccupied. In the [101] orientation the intensity variation of the A-site is due to the different partial occupancy of the A-site.
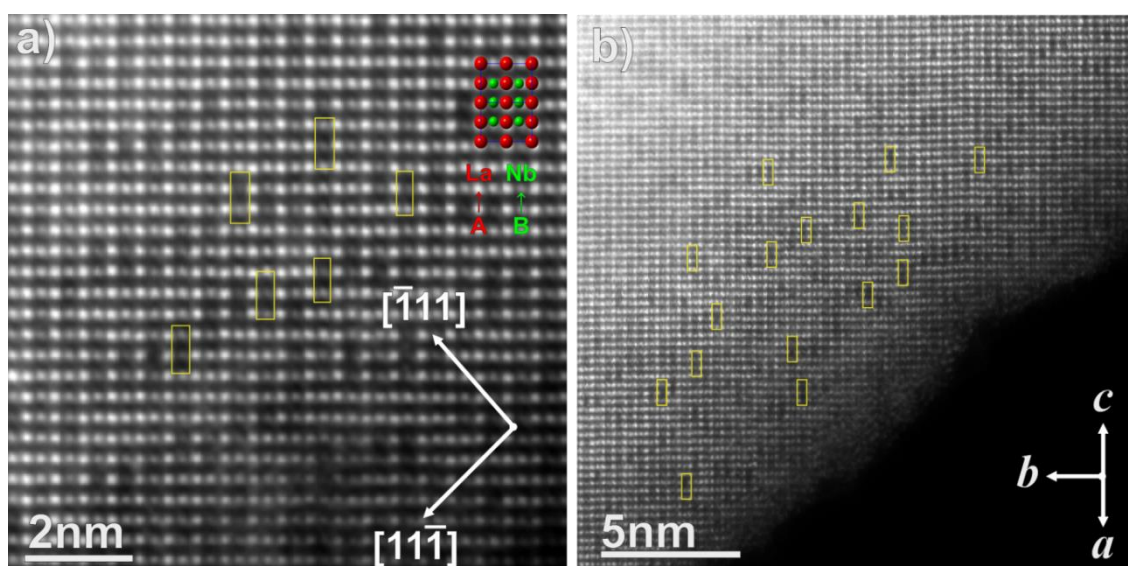

Figure S5: *a) HAADF STEM image (after rigid-registration of a stack of consecutive images), with overlaid ball-and-stick model of the Cmmm structure; b) HAADF STEM image of the LNO ceramic acquired along the [101] zone axis. Pairs of darker A-sites, marked by yellow rectangles, appear to align closely parallel to the $[\bar{1}11]$ and $[11\bar{1}]$ orientations.*

HAADF STEM images acquired along the [101] zone axis show that the intensity of the La columns can vary significantly from site to site (Figure S5), indicating a non-uniform distribution of A_1-site vacancies in the structure, which would not have been apparent from characterisation through bulk techniques only. Furthermore, the A-site columns with higher vacancy content appear to be paired (marked by yellow rectangles in Figure S5), and appear to be aligned closely parallel to the $[\bar{1}11]$ and $[11\bar{1}]$ crystallographic directions.

2.3. Electron Energy Loss Spectroscopy (EELS)

Local electronic structure variations can be fingerprinted through EELS analysis. The O *K* edge signal of LNO extracted from different regions of the structure (Figure S6a) shows differences in the near edge fine structure (ELNES): Figure S6b. In particular, a change in ratio of the peaks in ELNES marked as A and B (Figure S6b) is observed. By analogy to similar systems, the A and B peak typically arise from transitions to the unoccupied O *2p* states hybridising with the Nb *4d* states and La *5d* states, respecively[8–11], as evidenced also by the overlay of the calculated pDOS against the experimental EELS spectra, shown in Figure

S6c. The different occupancy of these two distinct A sites is therefore reflected in a change in the O bonding environment.
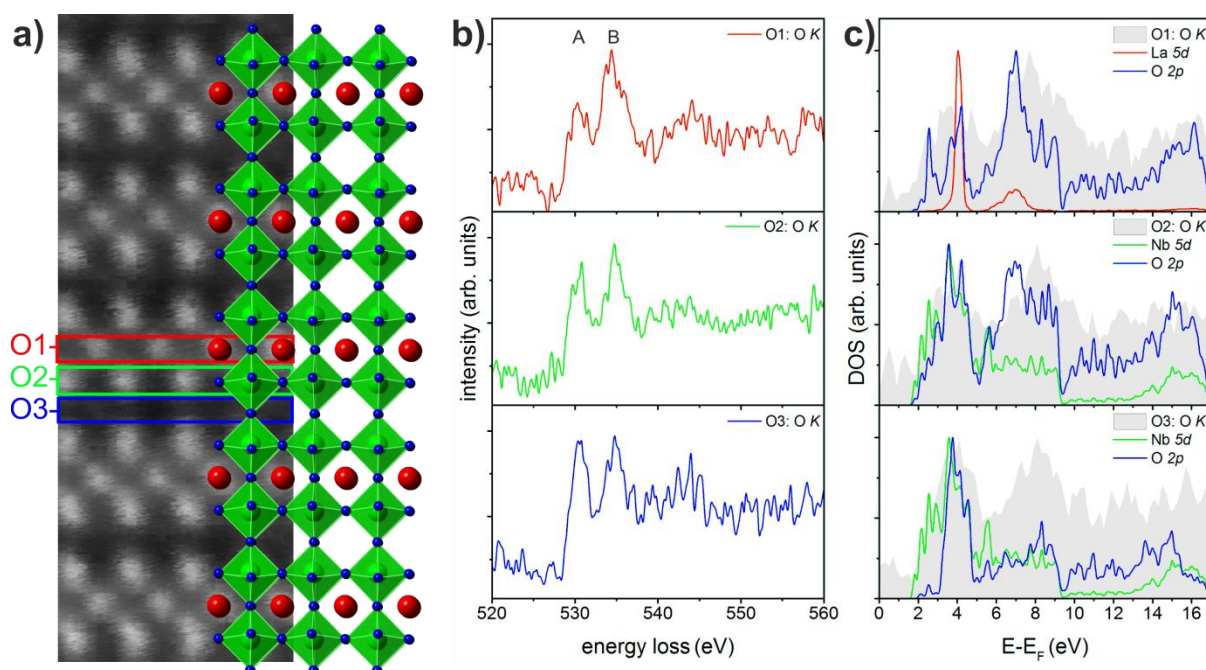

Figure S6: a) HAADF STEM signal and b) background subtracted O *K* EELS spectra from the regions marked in (a) and (c) calculated DOS of LNO projected onto La, Nb and O. The Fermi level is set at 0 eV. The pDOS is plotted against the experimental O *K* edges for the corresponding layers (as defined in Figure 12a). For reading clarity, the experimental spectra were rigidly translated to the site projected pDOS; no stretching of the energy axis was applied.

The optical bandgap of the LNO ceramic was determined by monochromated valence EELS measurements using a Nion UltraSTEM100MC–'HERMES' dedicated STEM[12], which is equipped with a high-resolution beam monochromator and a Gatan Enfinium spectrometer. The microscope was operated at 60 kV and at an energy spread of ~0.025 eV, as evidenced by the FWHM of the Zero Loss Peak (inset in Figure S7). According to Rafferty *et al.*[13] the valence EEL spectrum reflects the joint density of states of the material, and direct and indirect band gap onsets can be described by a parabolic or exponential function, respectively. The exponential shape of the spectrum onset observed on LNO (Figure S7) shows that the optical gap is dominated by indirect contributions, as expected from theoretical calculations. The value of the optical bandgap of LNO was determined from the intersection of the energy axis with a straight line fitted to the spectrum after the spectrum onset[14] (Figure S5), yielding a bandgap value of $E_g \sim 3.86$ eV.
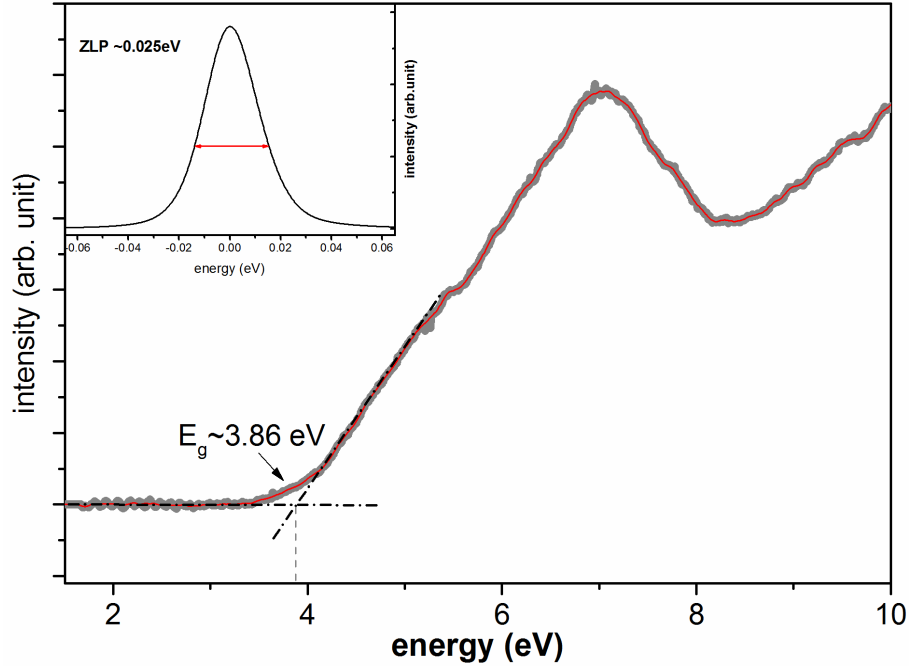
Figure S7: *Monochromated valence EELS measurement of the LNO ceramic, showing the determination of the band gap.*

3. Computational details:

3.1 Crystallographic model of $La_{1/3}NbO_3$ used in the calculations.

To initially model the average crystallographic structure of $La_{1/3}NbO_3$ a super cell comprising three primitive unit cells of $La_{1/3}NbO_3$ of *Cmmm* symmetry was used. All internal and lattice degrees of freedom were allowed to relax, and no symmetry constraints were applied during the calculations. After relaxation, a new primitive unit cell was identified of P*2/m* space group ($La_2Nb_6O_{18}$), which was 30 meV lower in energy than *Cmmm*. Thus in the electronic structure and transport calculations the P2/m unit cell as shown in Figure S6 was used. The lowering of the *Cmmm* symmetry to P2/m is related to the tilting of the NbO_6 octahedra as shown in Figure S8b. Note that this is the ground state configuration at 0 K, whereas the average experimental crystallographic structure was evaluated at room temperature.
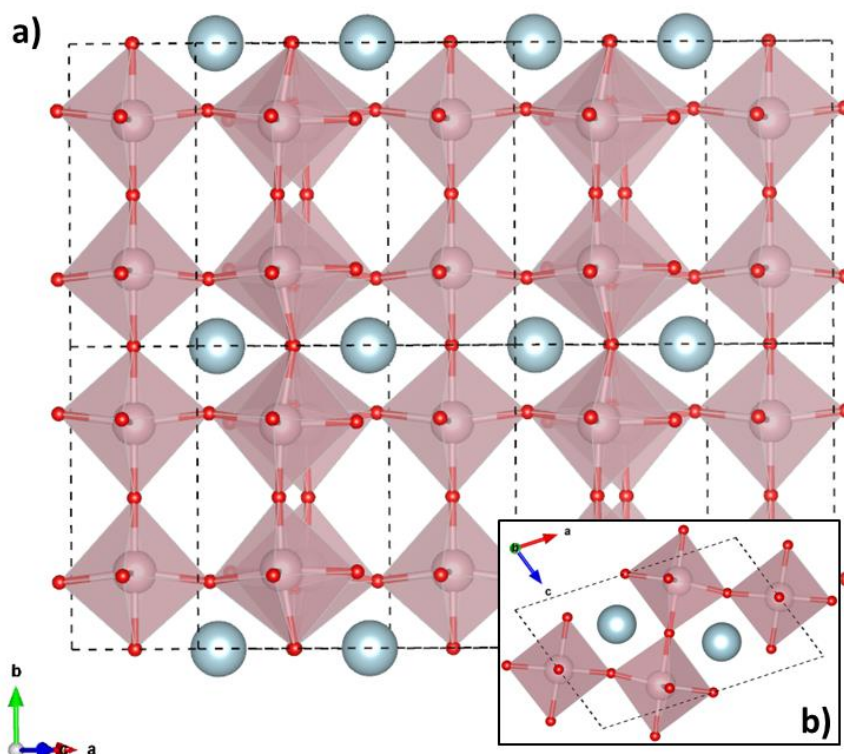
Supplementary Information:

Figure S8: *The structure of La$_{1/3}$NbO$_3$ (La$_2$Nb$_6$O$_{18}$) used in the evaluation of the electronic properties aligned showing projections perpendicular to (a) the ab and (b) the ac plane. The primitive unit cell is highlighted by the dashed lines.*

Table S2 lists corresponding primitive unit cell parameters of the La$_{1/3}$NbO$_3$ used in the calculations.

Table S2: PBE+*U* lattice parameters of the primitive cell of La$_{1/3}$NbO$_3$ with *P2/m* symmetry.

a (Å)	8.93586
b (Å)	8.06318
c (Å)	5.67636
V (Å)^3	388.13
α (∘)	90.0
β (∘)	71.62
γ (∘)	90.0

The calculated unit cell parameters when transformed into the orthorhombic unit cell representation are shown in Table S3.

Table S3: *PBE+U and MD lattice parameters of the La$_{1/3}$NbO$_3$ within the orthorhombic unit cell representation (α=β=γ=90˚).*

Lattice Parameters	MD	PBE+U
a (Å)	7.786	8.045
b (Å)	7.786	8.061
c (Å)	7.834	8.073
V (Å)^3	474.917	523.541

In the case of the MD calculations employing a classical force field as described in the methodology section, a very good agreement is obtained with the experimental data (see Table S1 and Table S3). The lattice parameters resulting from the PBE+U calculations compare also favourably to the experimental ones, although they point to a slightly elongated structure. This 'expansion' of the PBE+U calculated unit cell as compared to the experimental one is likely caused by the over localization of d-electrons in the calculation, which leads to an incorrect bond elongation.
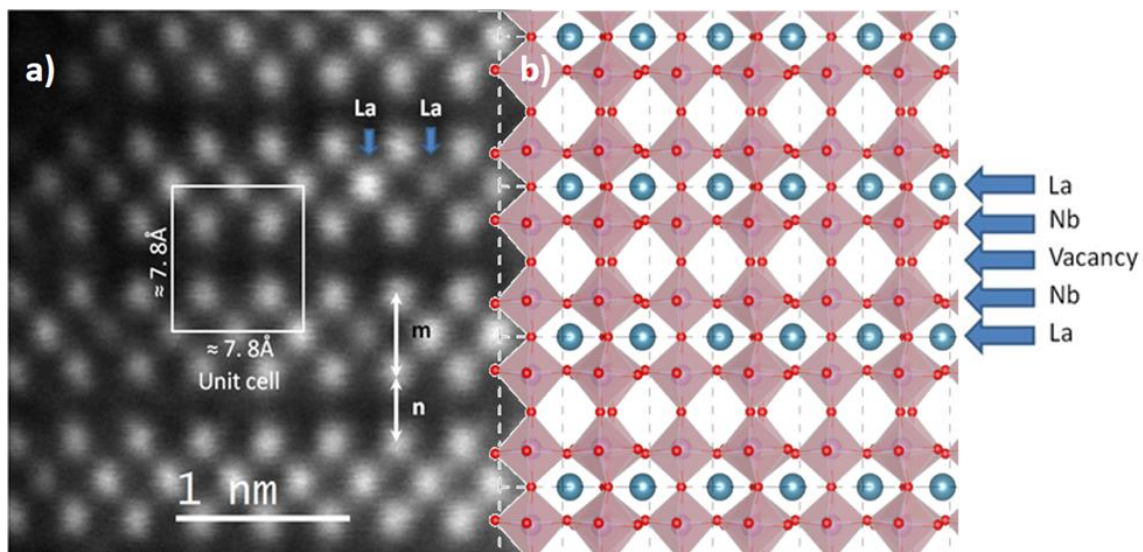

Figure S9: *a) [010] Experimental HAADF STEM image b) Optimized primitive unit cell of La$_{1/3}$NbO$_3$ resulted from PBE+U calculations. Colour code: Nb – purple, O – red, La – grey.*

3.2 Electronic transport.

The electronic transport was evaluated by solving the semi-classical Boltzmann transport equation within the relaxation time (τ) and the "rigid band approach" approximations as implemented in the BoltzTraP[15] program. Whereas the Seebeck coefficient can be calculated

on an absolute scale, all other transport properties including the electronic conductivity are known with respect to the relaxation time (τ).

As demonstrated in our previous work,[16] when the value of τ is chosen to be independent on temperature, it only applies a constant shift to the calculated conductivities. This is a good approximation for oxides as experimental evaluation of the relaxation time is not trivial and sample dependent. Figure S10 shows the corrected electrical conductivities as a function of carrier concentration for all the temperatures studied. The relaxation time τ, was chosen to be $8*10^{-19}$ s. This value allows for the best fit of the calculated electrical conductivities against the experimental measured data (Figure S11). The approximation holds well for temperatures higher than 500 K. This discrepancy may be due to the complexity of the experimental samples against a simple model used in our DFT calculations.
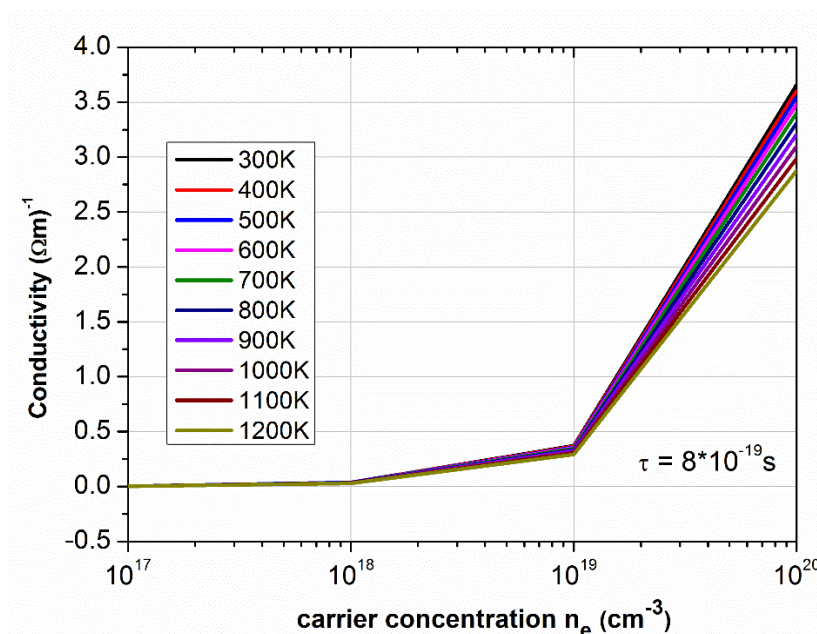

Figure S10: Corrected electrical conductivities as a function of carrier concentration for all the temperatures studied. The relaxation time τ, was chosen to be $8*10^{-19}$ s.

Cation doping is one of the main strategies to introduce charge carriers in thermoelectric oxides; calculations, shown in Figure S10 demonstrates how the introduction of charge carriers result in an increase electric conductivity. However, this strategy can be can be a double edged sword, as above a certain carrier concentration the Seebeck coefficient shows a linear decreasing tendency in magnitude, effectively balancing out the increase of conductivity in the thermopower ($S^2\sigma$). It should however be noted that our calculations

assume that doping does not change the shape of the band structure but only shifts the Fermi energy. More rigorous experimental and theoretical work would be necessary to access the exact effect of specific dopant concentration in the transport properties of the LNO ceramic.
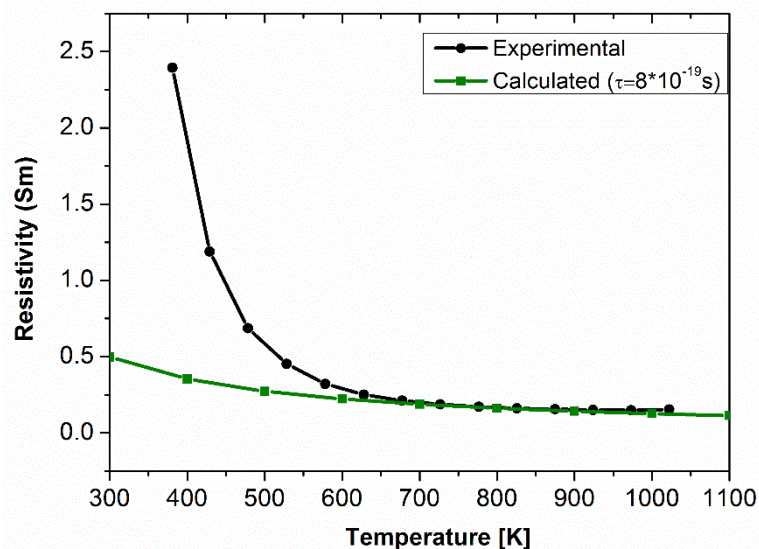

Figure S11: Best fit between the calculated and experimentally measured electrical conductivities (expressed as resistivity) as a function of temperature. The relaxation time τ, was chosen to be 8*10^{-19} s.

3.3 Note on the influence of the phase transition in the calculated transport properties

It should be noted that the electronic structure calculations did not specifically use two distinct structural models to avoid a discontinuity in the modelling results; both phases are wide band gap semiconductors as shown by experimental measurements of the band gap. The DFT results on the orthorhombic phase also show that the valence band and the conduction band are dominated by Nb and O states respectively in the density of states (Figure 7b of the main text). Furthermore, experimentally there is no anomalous behaviour of the conductivity vs. T (Figure 6a of the main text) at the transition temperature (480 K). These observations all suggests that the structural phase transition does not dramatically (discontinuously) change the density of states of LNO around the transition temperature. This motivated the use of a computational methodology, whereby a well-established approximation is taken to evaluate the TE properties as a function of temperature. The rigid band approximation within the

Boltzmann transport theory considers that there is only a broadening of the density of states at the conduction and valence bands, due to T effects as the temperature is increased. This however could be considered as providing a representation of the influence of the phase transition on the electronic structure around 480K, when the material goes from an orthorhombic to a tetragonal symmetry as a result of the rotation of the NbO_6 octahedra.

References

(1) Carrillo, L.; Villafuerte-Castrejón, M. E.; González, G.; Sansores, L. E.; Bucio, L.; Duque, J.; Pomés, R. Superstructure Determination of the Perovskite β $La_{0.33}NbO_3$. *J. Mater. Sci.* **2000**, *35*, 3047–3052 DOI: 10.1023/A:1004863715548.

(2) Kennedy, B. J.; Howard, C. J.; Kubota, Y.; Kato, K. Phase Transition Behaviour in the A-Site Deficient Perovskite Oxide $La_{1/3}NbO_3$. *J. Solid State Chem.* **2004**, *177*, 4552–4556 DOI: 10.1016/j.jssc.2004.08.047.

(3) Jones, L.; Yang, H.; Pennycook, T. J.; Marshall, M. S. J.; Van Aert, S.; Browning, N. D.; Castell, M. R.; Nellist, P. D. Smart Align—a New Tool for Robust Non-Rigid Registration of Scanning Microscope Data. *Adv. Struct. Chem. Imaging* **2015**, *1*, 8 DOI: 10.1186/s40679-015-0008-4.

(4) HREM Research. SmartAlign for Digital Micrograph. 2016, p https://www.hremresearch.com.

(5) Jones, L.; Nellist, P. D. Identifying and Correcting Scan Noise and Drift in the Scanning Transmission Electron Microscope. *Microsc. Microanal.* **2013**, *19*, 1050–1060 DOI: DOI: 10.1017/S1431927613001402.

(6) HREM Research. Jitterbug for Digital Micrograph. p https://www.hremresearch.com/.

(7) Barthel, J. Dr. Probe- STEM Simulation Software. 2016, p http://www.er-org/barthel/drprobe.

(8) de Groot, F. M. F.; Grioni, M.; Fuggle, J. C.; Ghijsen, J.; Sawatzky, G. A.; Petersen, H. Oxygen $1s$ X-Ray-Absorption Edges of Transition-Metal Oxides. *Phys. Rev. B* **1989**, *40*, 5715–5723.

(9) Azough, F.; Kepaptsoglou, D.; Ramasse, Q. M.; Schaffer, B.; Freer, R. On the Origin of Nanochessboard Superlattices in A-Site-Deficient Ca-Stabilized $Nd_{2/3}TiO_3$. *Chem. Mater.* **2015**, *27*, 497–507 DOI: 10.1021/cm5036985.

(10) Eberg, E.; van Helvoort, A. T. J.; Takahashi, R.; Gass, M.; Mendis, B.; Bleloch, A.; Holmestad, R.; Tybell, T. Electron Energy Loss Spectroscopy Investigation of Pb and Ti Hybridization with O at the $PbTiO_3/SrTiO_3$ Interface. *J. Appl. Phys.* **2011**, *109*, 34104 DOI: 10.1063/1.3544416.

(11) Bugnet, M.; Radtke, G.; Botton, G. A. Oxygen 1s Excitation and Tetragonal Distortion

from Core-Hole Effect in BaTiO3. *Phys. Rev. B* **2013**, *88*, 201107 DOI: 10.1103/PhysRevB.88.201107.

(12) Krivanek, O. L.; Lovejoy, T. C.; Murfitt, M. F.; Skone, G.; Batson, P. E.; Dellby, N. Towards Sub-10 meV Energy Resolution STEM-EELS. *J. Phys. Conf. Ser.* **2014**, *522*, 12023 DOI: 10.1088/1742-6596/522/1/012023.

(13) Rafferty, B.; Brown, L. M. Direct and Indirect Transitions in the Region of the Band Gap Using Electron-Energy-Loss Spectroscopy. *Phys. Rev. B* **1998**, *58*, 10326–10337 DOI: 10.1103/PhysRevB.58.10326.

(14) Bangert, U.; Harvey, A.; Davidson, J.; Keyse, R.; Dieker, C. Correlation between Microstructure and Localized Band Gap of GaN Grown on SiC. *J. Appl. Phys.* **1998**, *83*, 7726–7729 DOI: 10.1063/1.367945.

(15) Madsen, G. K. H.; Singh, D. J. BoltzTraP. A Code for Calculating Band-Structure Dependent Quantities. *Comput. Phys. Commun.* **2006**, *175*, 67–71 DOI: 10.1016/j.cpc.2006.03.007.

(16) Molinari, M.; Tompsett, D. A.; Parker, S. C.; Azough, F.; Freer, R. Structural, Electronic and Thermoelectric Behaviour of CaMnO 3 and CaMnO (3−δ). *J. Mater. Chem. A* **2014**, *2*, 14109–14117 DOI: 10.1039/C4TA01514B.